Spatially separating redox centers on 2D carbon nitride with cobalt single atom for photocatalytic H_2O_2 production

Chiheng Chu[a], Qianhong Zhu[a], Zhenhua Pan[b], Srishti Gupta[c], Dahong Huang[a], Yonghua Du[d], Seunghyun Weon[a], Yueshen Wu[e], Christopher Muhich[c], Eli Stavitski[d], Kazunari Domen[b,f], and Jae-Hong Kim[a,1]

[a]Department of Chemical and Environmental Engineering, Yale University, New Haven, CT 06511; [b]Department of Chemical System Engineering, School of Engineering, The University of Tokyo, Bunkyo-ku, Tokyo 113-8656, Japan; [c]School for the Engineering of Matter, Transport, and Energy, Arizona State University, Tempe, AZ 85281; [d]National Synchrotron Light Source II, Brookhaven National Laboratory, Upton, NY 11973; [e]Department of Chemistry, Yale University, New Haven, CT 06511; and [f]Research Initiative for Supra-Materials, Shinshu University, Nagano 380-8553, Japan

Edited by Richard Eisenberg, University of Rochester, Rochester, New York, and approved February 13, 2020 (received for review August 3, 2019)

Redox cocatalysts play crucial roles in photosynthetic reactions, yet simultaneous loading of oxidative and reductive cocatalysts often leads to enhanced charge recombination that is detrimental to photosynthesis. This study introduces an approach to simultaneously load two redox cocatalysts, atomically dispersed cobalt for improving oxidation activity and anthraquinone for improving reduction selectivity, onto graphitic carbon nitride (C_3N_4) nanosheets for photocatalytic H_2O_2 production. Spatial separation of oxidative and reductive cocatalysts was achieved on a two-dimensional (2D) photocatalyst, by coordinating cobalt single atom above the void center of C_3N_4 and anchoring anthraquinone at the edges of C_3N_4 nanosheets. Such spatial separation, experimentally confirmed and computationally simulated, was found to be critical for enhancing surface charge separation and achieving efficient H_2O_2 production. This center/edge strategy for spatial separation of cocatalysts may be applied on other 2D photocatalysts that are increasingly studied in photosynthetic reactions.

2D photocatalyst | spatially separated cocatalysts | single-atom catalyst | hydrogen peroxide

Harvesting solar photon energy to drive redox reactions involving water and oxygen is the most espoused strategy for the green synthesis of alternative fuels such as H_2 and H_2O_2 (1–4). Yet, solar-to-energy conversion efficiencies achieved using current semiconductor photocatalysts remain relatively low (5, 6), due to inherent limitations in material properties such as prevalent charge recombination in low-bandgap materials and the insufficient selectivity toward the fuel synthesis reaction (7). One promising material engineering strategy is to decorate the semiconductor surface with cocatalysts (1, 8), ideally both reductive and oxidative cocatalysts within a single photocatalytic material. Nevertheless, randomly loading two cocatalysts often results in direct contact between oxidation and reduction centers, worsening the charge recombination that is detrimental to photosynthetic reactions (Fig. 1*A*) (9).

Placing two cocatalysts without direct contact requires sophisticated material architecture and synthesis strategy. One cocatalyst, typically oxidative, can be loaded on a substrate in trace amounts to minimize such contact but only at the expense of the available catalytic sites and thus the overall efficiency (10, 11). A more promising strategy is to design the substrate photocatalysts to provide physically separated sites for cocatalyst hosting. For instance, Wang et al. (9) recently fabricated a core/shell photocatalyst that can host reductive and oxidative cocatalysts separated inside and outside of the shell surfaces (Fig. 1*B*). Following this seminal work, various core/shell structures have been prepared, which typically require complicated synthesis procedures involving the use of sacrificial templates (e.g., SiO_2) (12–15). Alternatively, different facets of photocatalytic materials were found to selectively load different cocatalysts, allowing spatial segregation (Fig. 1*C*) (16–18).

The existing strategies to prepare spatially separated cocatalysts, however, exclusively rely on the three-dimensional nature of the substrate structure and cannot be readily extended to 2D materials such as graphitic carbon nitride (C_3N_4). C_3N_4 has often been used as the semiconductor material of choice for the photocatalytic synthesis of H_2O_2 (3, 19, 20), an emerging substitute for compressed H_2 due to recent advances in H_2O_2 fuel-cell technology (21). C_3N_4 exhibits valence-band (VB) and conduction-band (CB) potentials that span those of H_2O/O_2 and H_2O_2/O_2 redox pairs and is capable of harnessing broad spectrum of sunlight due to its low-bandgap energy. However, solar-to-fuel conversion efficiencies remain, in general, relatively low due to limitations that are commonly found in other materials: 1) ineffective hole scavenging via water oxidation and the resulting charge recombination (3, 19), which often necessitates the addition of organic electron donors (22–25), and 2) low selectivity toward H_2O_2 synthesis via two-electron reduction of O_2 ($O_2 + 2H^+ + 2e^- \rightarrow H_2O_2$) as compared to four-electron reduction of O_2 ($O_2 + 4H^+ + 4e^- \rightarrow 2H_2O$) or two-electron H_2 evolution ($2H^+ + 2e^- \rightarrow H_2$) (3, 19).

Here we introduce an innovative strategy to load two cocatalysts onto 2D C_3N_4, with controlled physical separation in atomistic scale (Fig. 1*D*). We use cobalt and anthraquinone (AQ) as cocatalysts that are crucial for efficient photocatalytic synthesis

Significance

Photocatalysts frequently require simultaneous loading of oxidative and reductive cocatalysts to achieve both efficient half-reactions within a single material. Nevertheless, unregulated loading and distribution of two cocatalysts will result in direct contact between oxidation and reduction centers, leading to detrimental charge recombination. This research presents a center/edge approach to load two redox cocatalysts with controlled physical separation in atomistic scale using single-atom architecture. This spatial separation is critical for enhancing surface charge separation and achieving efficient H_2O_2 production. We report that redox cocatalysts are spatially separated on a two-dimensional (2D) photocatalyst, which opens an approach for achieving both efficient oxidation and reduction reactions on 2D photocatalysts.

Author contributions: C.C., Q.Z., S.G., D.H., C.M., E.S., K.D., and J.-H.K. designed research; C.C., Q.Z., Z.P., S.G., Y.D., S.W., and Y.W. performed research; C.C. contributed new reagents/analytic tools; C.C., Q.Z., Z.P., S.G., D.H., S.W., Y.W., C.M., E.S., K.D., and J.-H.K. analyzed data; and C.C., Q.Z., S.G., C.M., E.S., and J.-H.K. wrote the paper.

The authors declare no competing interest.

This article is a PNAS Direct Submission.

See online for related content such as Commentaries.

[1]To whom correspondence may be addressed. Email: jaehong.kim@yale.edu.

This article contains supporting information online at https://www.pnas.org/lookup/suppl/doi:10.1073/pnas.1913403117/-/DCSupplemental.

First published March 11, 2020.

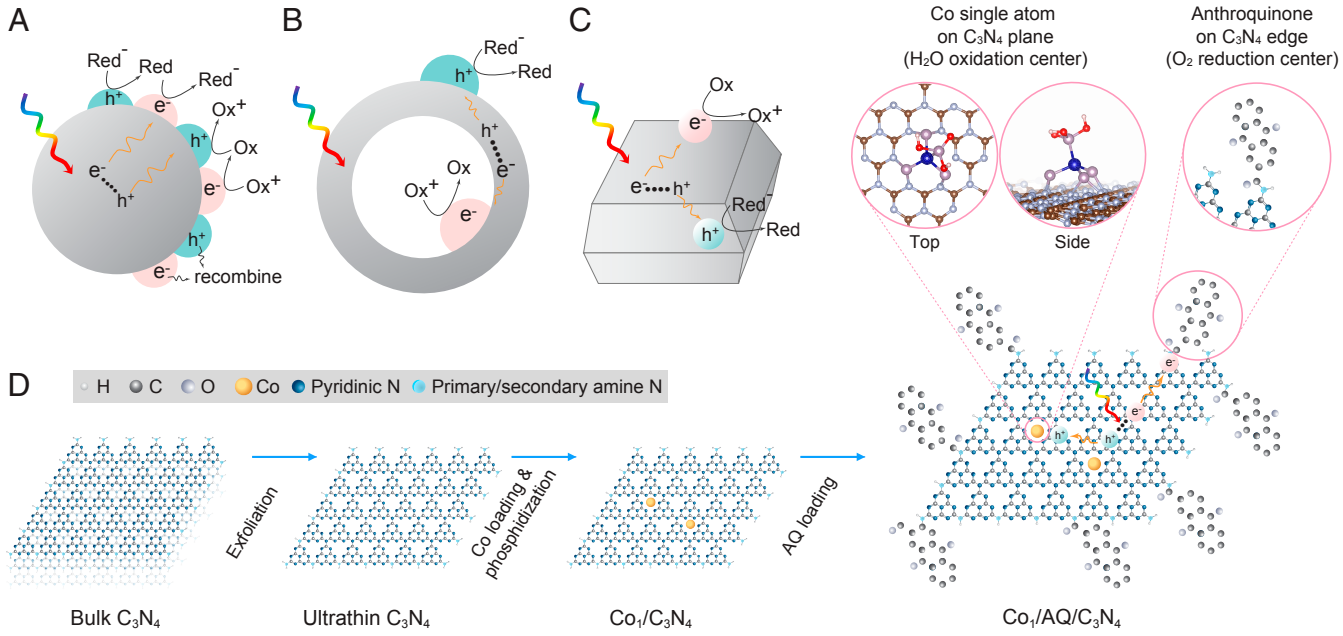

Fig. 1. (*A*) Randomly loading two cocatalysts leads to detrimental sequences of reactions involving oxidant (Ox) and reductant (Red). (*B*) Core/shell structured photocatalysts and (*C*) photocatalysts with different exposed crystalline facets to achieve controlled spatial separation of oxidative and reductive cocatalysts. (*D*) Spatial separation of Co single atom (as oxidation center) and AQ (as reduction center) cocatalysts by anchoring them in the center (i.e., pyridinic N) and on the edge (i.e., primary/secondary amine N) of 2D ultrathin C_3N_4, respectively.

of H_2O_2. Co is anchored to void center of the C_3N_4 as a single atom (Co_1) and serves to facilitate the water oxidation (26–30). At the same time, AQ is attached to amine anchors that are present only on the edge of C_3N_4, ensuring that it is not in direct contact with the Co centers. The AQ enhances the selectivity of O_2 reduction to H_2O_2, following the mechanism widely exploited in current industrial H_2O_2 production process (31). The composite catalyst, $Co_1/AQ/C_3N_4$, photocatalytically produces H_2O_2 at high efficiency under simulated solar irradiation without the supply of a sacrificial agent.

We first prepared ultrathin C_3N_4 nanosheets by exfoliating bulk C_3N_4 under probe sonication (32). The C_3N_4 nanosheets

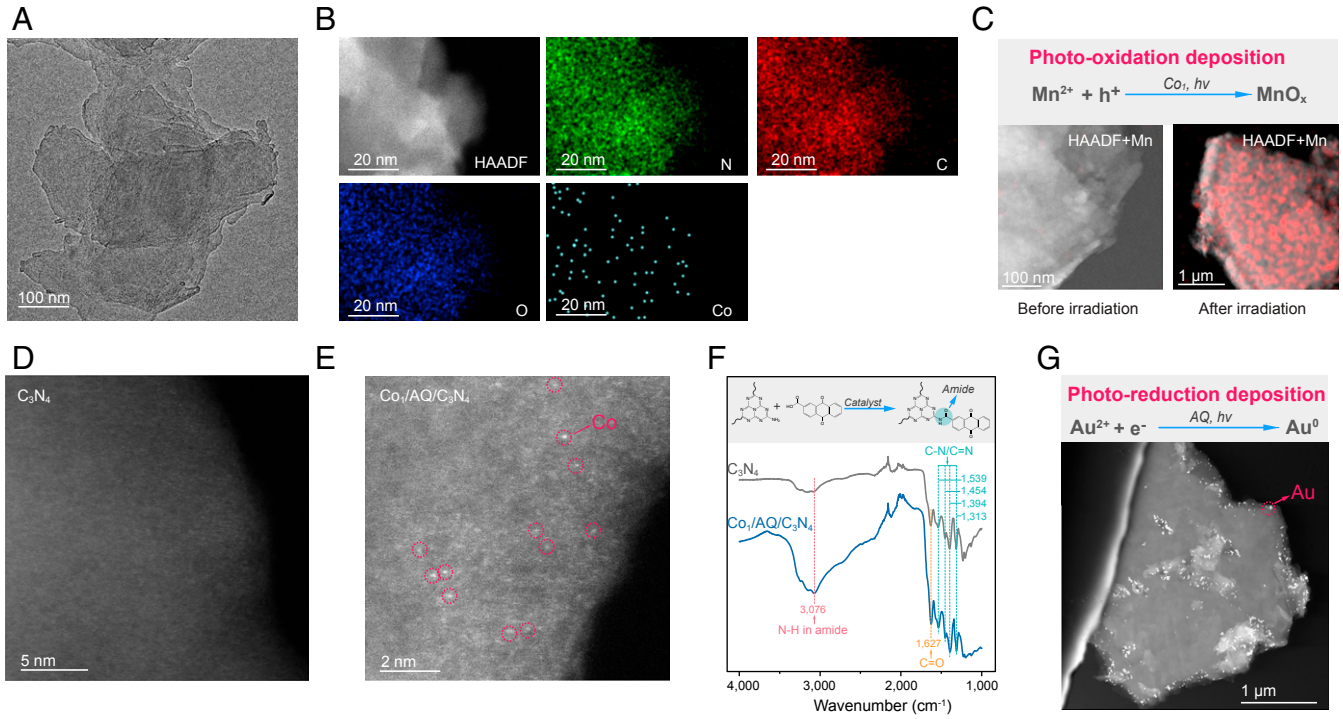

Fig. 2. (*A* and *B*) HRTEM and EDS images of $Co_1/AQ/C_3N_4$. (*C*) Photooxidative deposition of Mn on Co_1/C_3N_4. (*D* and *E*) HAADF-STEM image of C_3N_4 and $Co_1/AQ/C_3N_4$. (*F*) FT-IR spectra of C_3N_4 and $Co_1/AQ/C_3N_4$. (*G*) Photoreductive deposition of Au on AQ/C_3N_4.

appeared to be only a few layers thick according to high-resolution transmission electron microscopy (HRTEM) images (Fig. 2*A*). We then loaded Co onto the ultrathin C_3N_4 using a two-step synthesis: attachment of Co precursors to anchor sites followed by pyrolysis (33). Co ions are attached to the void center of C_3N_4 nanosheets through forming stable coordination with pyridinic N atoms in surrounding heptazine units of C_3N_4 (Fig. 1*D*), as suggested by this site having the lowest relative energy (34, 35). After pyrolysis under N_2 atmosphere, Co ions were further phosphodized under PH_3 atmosphere to enhance their activity for water oxidation (26, 33, 36).

Energy-dispersive X-ray spectroscopy (EDS) elemental mapping suggests that Co is uniformly distributed across the C_3N_4 surface (Fig. 2*B*). To further provide a visual confirmation, we photooxidatively deposited Mn^{2+} to grow MnO_x nanoparticles ($Mn^{2+} + xH_2O + [2x\text{-}2]h^+ \rightarrow MnO_x + 2xH^+$) on Co as seed sites (16, 37, 38). The formation of MnO_x across the C_3N_4 surface readily observed by low-resolution TEM (Fig. 2*C*) suggests that Co atoms are also distributed across the C_3N_4 surface and serve as oxidation centers. High-angle annular dark-field scanning transmission electron microscopy (HAADF-STEM) images indicates that the Co is likely atomically dispersed [Fig. 2*E* as compared to C_3N_4 before Co loading (Fig. 2*D*)], since the radii of Co were estimated to be ~0.5 Å. Notably, all Co single atoms identified were located at least ~1 nm away from the edge of C_3N_4 (Fig. 2*E* and *SI Appendix*, Fig. S2), indicating the selective loading of Co on the surface, not the edge, of C_3N_4 nanosheet.

Consistent with the absence of Co metallic clusters in HAADF-STEM images, another strong piece of evidence for the atomic dispersion of Co is provided by the absence of Co-Co coordination in K-edge spectrum from Fourier-transformed extended X-ray absorption fine-structure spectroscopy (FT-EXAFS, Fig. 3*A*). The spectrum also indicates that Co atoms are primarily coordinated by P (i.e., peak at 1.8 Å in FT-EXAFS) (33), which confirms the complete phosphidation. The coordination with P is further supported by the occurrence of a prominent Co-P peak at 129.6 eV in the X-ray photoelectron spectroscopy (XPS) spectrum (Fig. 3*D*). A P-N peak at 133.6 eV also suggests that P atoms coordinate with N atoms in heptazine rings of C_3N_4. Best-fit parameters extracted from the FT-EXAFS spectra (Fig. 3*B*) suggest an average Co-P coordination distance at 2.29 Å and coordination number of 4.1 (*SI Appendix*, Table S1), consistent with previous observations (33). Co atoms are found to be positively charged with partially unoccupied 3d orbitals. Comparison of the Co K-edge normalized near-edge X-ray absorption spectroscopy (XANES) of $Co_1/AQ/C_3N_4$ with those of reference compounds shows that the spectral line shape and the absorption edge position closely resemble those of CoO (Fig. 3*C*), indicating that the oxidation state of the Co single atoms is close to +2. Density-functional theory calculations (DFT; see *SI Appendix*, section S6 for details) confirm that Co atoms are positively charged. The above results collectively suggest that Co cocatalysts are uniformly loaded in the center of C_3N_4 nanosheet as positively charged single atoms.

XAFS measurements at the P K-edge further provide a clue on the structure of Co single atom and its surrounding. EXAFS spectrum at the P K-edge indicates that P atoms are primarily coordinated by Co atoms (i.e., peak at 1.87 Å in FT-EXAFS;

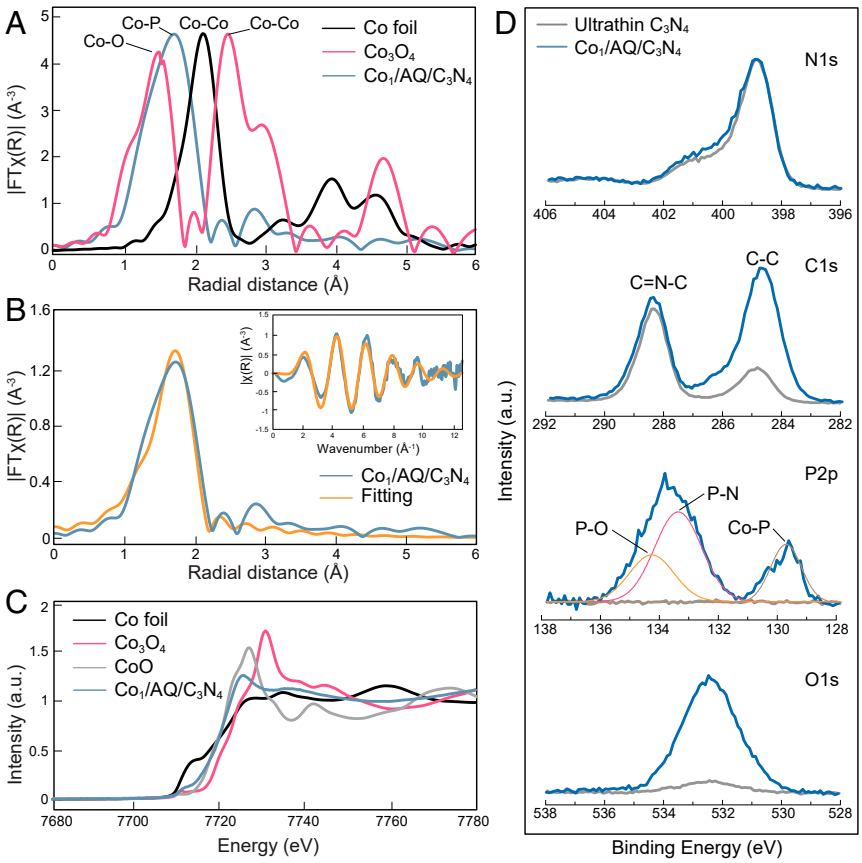

Fig. 3. (*A*) FT EXAFS spectra of $Co_1/AQ/C_3N_4$ at the Co K edge. The intensity of Co_3O_4 and $Co_1/AQ/C_3N_4$ was normalized to the same maximum of Co foil to facilitate the comparison of radical distances by multiplying with a factor of 2.1 and 3.6, respectively. (*B*) Fit of $Co_1/AQ/C_3N_4$ EXAFS spectra using Co foil and Co_3O_4. (*Inset*) Corresponding K-space curves. (*C*) Normalized XANES of $Co_1/AQ/C_3N_4$ at the Co K edge. (*D*) Binding energy of N 1s, C 1s, P 2p, and O 1s for ultrathin C_3N_4 and $Co_1/AQ/C_3N_4$ by high-resolution XPS.

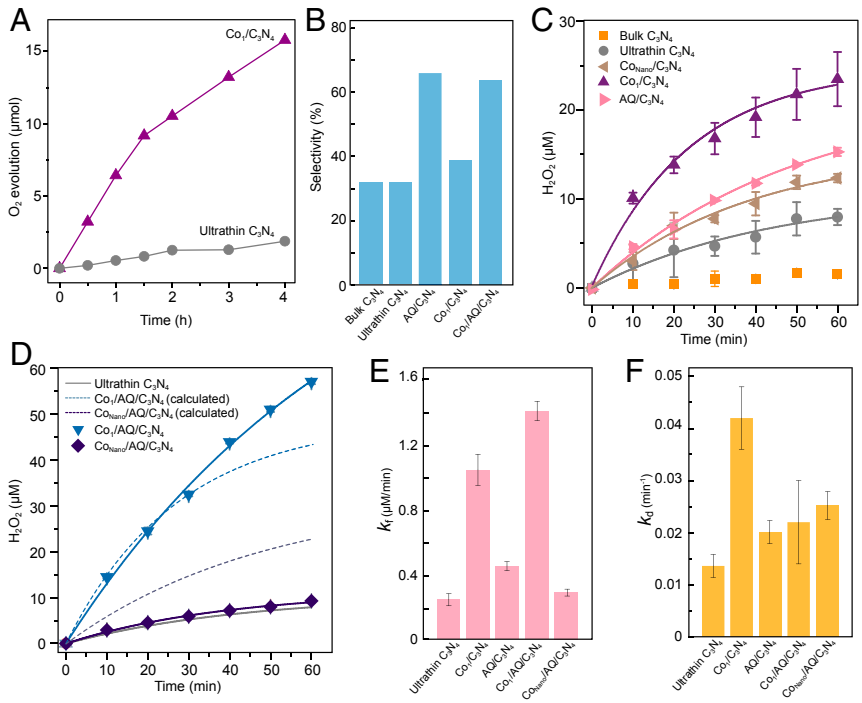

Fig. 4. (*A*) Time course of O_2 evolution measured under 0.6-kPa Ar pressure and 300-W xenon lamp irradiation with 0.5 g/L of catalyst, 1 g/L La_2O_3, and 20 mM $AgNO_3$ in 100 mL water. (*B*) Selectivity of H_2O_2 production. (*C* and *D*) Time course of H_2O_2 production measured under simulated sunlight irradiation (xenon lamp solar simulator, 100 mW/cm^2, AM 1.5G) with 0.5 g/L of catalyst under O_2-saturated condition. Solid lines are the fitting result of the kinetic model. Dotted lines are H_2O_2 productions estimated assuming additive enhancement of each cocatalyst. (*E* and *F*) H_2O_2 formation and decomposition rate constants. Error bars represent the SDs of triplicates.

SI Appendix, Fig. S3*A*), which is consistent with the corresponding FT-EXAFS data recorded at Co K-edge (Fig. 3*B*). These P atoms are further coordinated with N atoms in heptazine rings of C_3N_4 as well as O atoms, as evidenced by P-N peak at 133.5 eV and P-O peak at 134.5 eV in XPS spectrum (Fig. 3*D*). XANES spectrum at the P K-edge shows that the preedge region is dominated by the strong feature at 2,143.6 eV, which is assigned to low-valence phosphidic species (*SI Appendix*, Fig. S3*B*) (39). The higher-energy, broader peak centered around 2,152.0 eV is consistent with high-valence P (*SI Appendix*, Fig. S3*B*) (40). Comparison of intensities of the two maxima suggests that 20–30% of the phosphorus atoms exist in high-valence state. Alternatively speaking, Co atoms are coordinated with three low-valence P atoms (i.e., coordinated with N atoms in heptazine rings of C_3N_4) and one high-valence P atom (i.e., coordinated with O atoms). Geometry optimization conducted under these constraints using DFT confirms that the proposed Co center structure is stable (Fig. 1*D*, top and side view of Co center), in which Co is placed out of C_3N_4 plane. Other configurations, particularly in-plane P substitutions and Co insertions, resulted in sheet disintegration or massive structural rearrangement.

Loading Co single atoms significantly enhanced C_3N_4 for water oxidation ($2H_2O \rightarrow O_2 + 4H^+ + 4e^-$), as indicated by an

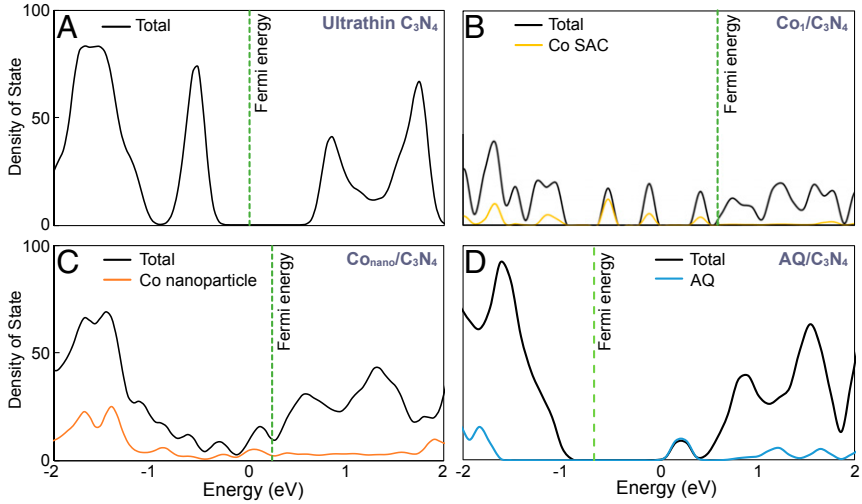

Fig. 5. Density of states computed with DFT for (*A*) C_3N_4, (*B*) C_3N_4 loaded with Co single atom cocatalyst (SAC), (*C*) C_3N_4 loaded with Co nanoparticle (showing Co_4 as an example), and (*D*) Co loaded with AQ.

8.4-fold enhancement on 4-h O_2 production (Fig. 4*A* and see *SI Appendix*, section S5 for details). According to our DFT calculations (see *SI Appendix*, section S6 for details), the enhanced water oxidation is attributed to strong adsorption of water molecule on Co single atom (exothermic by 2.7 eV when replacing the phosphite moiety), while no adsorption is observed on the plane C_3N_4 sheet. In addition, atomically dispersed Co produces two distinct, occupied, midgap states ~0.5 and 0.9 eV above the VB maximum when the H_2O is absorbed, promoting the localization of photoexcited holes and subsequent charge separation (Fig. 5 *A* and *B*), whereas Co nanoparticles completely fill the bandgap and thus act as charge recombination centers (Fig. 5*C*). All of these results indicate that Co loading enhances the hole quenching by water and therefore the overall charge-separation, i.e., more electrons are available for the reductive H_2O_2 synthesis.

Secondly, we loaded AQ cocatalyst onto Co_1/C_3N_4 by forming amide bonds between carboxylic groups in anthraquinone-2-carboxylic acid and primary/secondary amine groups on the edge of C_3N_4 (Fig. 1*D*) (8, 35). Successful loading of AQ was confirmed by XPS in which $Co_1/AQ/C_3N_4$ exhibits strong peak corresponding to C-C fragments (284.7 eV) that mostly originate from AQ molecules (Fig. 3*D*). The AQ molecules remained bound to C_3N_4 after intensive solvent washing, suggesting that they are chemically attached rather than physically adsorbed (23). The successful loading of AQ was also confirmed by Fourier-transform infrared spectroscopy (FT-IR) spectroscopy. As shown in Fig. 2*F*, the intensities of the FT-IR peaks corresponding to the amide functionalities, including the C=O stretching vibration peak at 1627 cm^{-1} and the N-H stretching vibration peak at 3,076 cm^{-1}, increased dramatically with AQ loading. The quantitative analysis of XPS spectra indicates that AQ was loaded at 16% (wt/wt).

To provide a visual confirmation of the site-selective loading of AQ, we photoreductively deposited noble metals by reducing metal precursors (i.e., H_2AuCl_4 or H_2PtCl_6) on AQ as seed sites ($M^{n+} + ne^- \rightarrow M^0$) (16). TEM images clearly showed that the Au and Pt nanoparticles were selectively deposited on the edge of C_3N_4 nanosheets (Fig. 2*G* and *SI Appendix*, Figs. S4 and S5), which were in stark contrast to random deposition of Au nanoparticles on pristine C_3N_4 surface without AQ functionality (*SI Appendix*, Fig. S6) (41). These results confirm that AQ cocatalysts were selectively loaded on the edge of C_3N_4 nanosheets and serve as reduction center. DFT calculations confirmed the electron withdrawal by the AQ cocatalyst, where AQ molecule generates an empty state that is only 0.3 eV below the CB of C_3N_4; while filled AQ states, where a hole would occupy, sits more than 0.8 eV below the VB of C_3N_4 (Fig. 5*D*). Therefore, transfer of a photoexcited electron to AQ is allowed but transfer of a photoexcited hole is prohibited, leading to enhanced charge separation.

Loading AQ cocatalyst onto C_3N_4 had a significant impact on enhancing the selectivity of H_2O_2 synthesis from ~30% by pristine C_3N_4 to over 60% (Fig. 4*B*); H_2O_2 production selectivity is defined as the ratio of electrons utilized for H_2O_2 synthesis to the total number of electrons consumed (*SI Appendix*, section S3 and ref. 22). In contrast, C_3N_4 exfoliation or Co loading had limited impact on H_2O_2 production selectivity (Fig. 4*B*). The enhanced H_2O_2 production selectivity is attributed to the two-step reaction catalyzed by AQ: 1) reductive hydrogenation of AQ to hydroxyanthraquinone (AQH_2) utilizing 2 e^- from photoexcited C_3N_4 followed by 2) H_2O_2 formation from concurrent oxygen reduction and dehydrogenation of AQH_2 back to AQ (*SI Appendix*, Fig. S7).

The photocatalytic H_2O_2-production performance of the as-prepared catalysts was evaluated under simulated sunlight irradiation in the absence of organic electron donor. Exfoliation of bulk C_3N_4 to nanosheets enhanced the photocatalytic H_2O_2 production performance of C_3N_4 (Fig. 4*C*) due to a larger number of exposed reaction sites and improved light-harvesting capability (8, 32). The light-harvesting capability of C_3N_4 was further improved with Co loading, as indicated by the lowered bandgaps [refer to the band-structure diagram (*SI Appendix*, Fig. S8)] constructed from XPS valence spectra (*SI Appendix*, Fig. S9) and diffuse reflectance spectra (*SI Appendix*, Fig. S10). Co cocatalyst loading promoted the water oxidation reaction and consequentially reduced detrimental exciton recombination (26, 33, 34, 42), leading to enhanced H_2O_2 production (Fig. 4*C*). For instance, when Co was loaded as nanoparticles (see *SI Appendix*, section S2 for synthesis details), i.e., not as single atoms, H_2O_2 production was enhanced, albeit slightly; when Co was loaded as single atoms, H_2O_2 production was enhanced by 4.0-fold. On the other hand, loading AQ cocatalyst onto ultrathin C_3N_4 improved H_2O_2 production selectivity, resulting in a 1.9-fold enhancement in H_2O_2 production (Fig. 4*C*).

Simultaneous loading of Co single atoms and AQ cocatalyst significantly enhanced H_2O_2 production by a factor of 7.3 (Fig. 4*D*). For the solar photocatalytic H_2O_2 production performed in the absence of electron donor, the initial production rate of 62 μM/h (apparent quantum efficiency = 0.054% over the full spectrum of sunlight; see *SI Appendix*, sections S8 and S9 for calculation details) and the cumulative production of 230 μM over 8-h period (*SI Appendix*, Fig. S11) achieved by $Co_1/AQ/C_3N_4$ in this study are among the highest reported (*SI Appendix*, Table S2) (43, 44). When the suspension was N_2-purged, the H_2O_2 production was mostly inhibited, confirming that O_2 reduction was the major pathway for H_2O_2 production (*SI Appendix*, Fig. S12). The stability of $Co_1/AQ/C_3N_4$ was demonstrated by its stable catalytic performance through repetitive use up to five cycles (*SI Appendix*, Fig. S13). XPS (*SI Appendix*, Fig. S14) and TEM (*SI Appendix*, Fig. S15) analyses show no significant change in chemical composition or ultrathin layered structure of $Co_1/AQ/C_3N_4$ after 8-h irradiation. We note that a better intersheet packing control may be achieved by immobilizing $Co_1/AQ/C_3N_4$ to facilitate its application in large-scale photolysis device setup (43, 44).

The enhancement on H_2O_2 production by coloading of Co single atoms and AQ is close to the multiplication of individual enhancements (Fig. 4*D*); i.e., the 4.0-fold enhancement by Co single atom cocatalyst times the 1.9-fold enhancement by AQ cocatalyst is close to the observed 7.3-fold enhancement on 60-min H_2O_2 production. This collaborative effect suggests that two cocatalysts contribute to H_2O_2 production enhancement independently without any negating effect. In contrast, when Co was loaded as nanoparticles onto AQ-C_3N_4, H_2O_2 production was much lower than that expected by considering the individual effects of Co nanoparticles and AQ (i.e., the observed 1.2-fold enhancement is much lower than the 1.5-fold enhancement by Co nanoparticle times the 1.9-fold enhancement by AQ on 60-min H_2O_2 production; Fig. 4*D*). This is due to random distribution of large Co particles across C_3N_4 and likely contact between Co cocatalyst and AQ cocatalyst. Such a contact would facilitate direct electron transfer without H_2O_2 evolution or water splitting (Fig. 1*A*). Loading Co as single atom, in contrast, ensures that Co is spatially separated from AQ. Since Co atom occupies the void center of C_3N_4 and AQ is located only at the edge of C_3N_4, molecular structure of C_3N_4 inherently maintains their separations at the minimum of 0.8 nm (*SI Appendix*, Fig. S16). Consistently, the steady-state photoluminescence from $Co_1/AQ/C_3N_4$ was markedly reduced compared not only to C_3N_4 but also to $Co_{nano}/AQ/C_3N_4$, indicating that the radiative recombination is more effectively retarded with Co single atom than Co nanoparticle (Fig. 6*A*). Time-resolved photoluminescence (TRPL, Fig. 6*B*) analyses show that the lifetime of excited-state $Co_1/AQ/C_3N_4$ (1.73 ns) is shorter than that of C_3N_4 (3.23 ns) and $Co_{-Nano}/AQ/C_3N_4$ (2.23 ns), highlighting the improved photoexciton dissociation in $Co_1/AQ/C_3N_4$ that was realized by spatial separation of AQ and Co single atoms.

We further analyze the H_2O_2 production by evaluating the rate of H_2O_2 formation (k_f) separately from the rate of H_2O_2 decomposition (k_d) (see *SI Appendix*, section S7 for the kinetic analysis). The results show that H_2O_2 formation rate constant increased upon individual loading of Co single atom, Co nanoparticle, or AQ. While

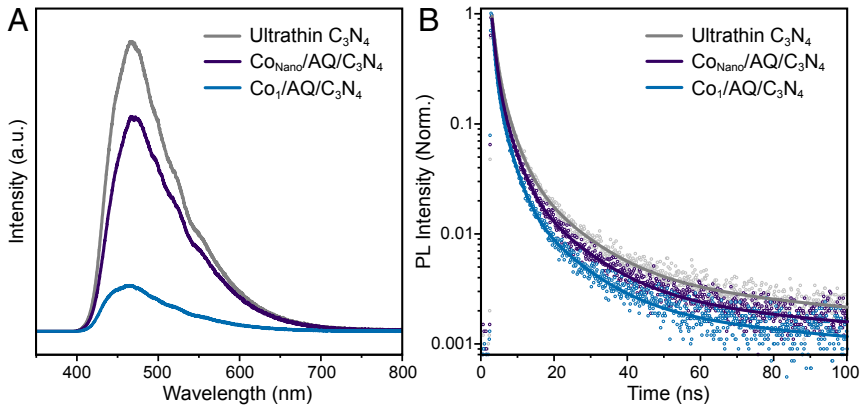

Fig. 6. (*A*) Steady-state PL emission spectra (excitation at 375 nm) of C_3N_4, $Co_{nano}/AQ/C_3N_4$, and $Co_1/AQ/C_3N_4$. (*B*) TRPL spectra monitored for entire emission between 400 and 800 nm. The curves were fitted to the equation $y = y_0 + A_1 \exp(-t/\tau_1) + A_2 \exp(-t/\tau_2) + A_3 \exp(-t/\tau_3)$.

simultaneous loading of Co single atom and AQ lead to additive enhancement on k_f, simultaneous loading of Co nanoparticle and AQ had an antagonistic effect on k_f (Fig. 4*E*), once again highlighting the importance of controlled physical separation between Co and AQ. It is also noteworthy that Co may negatively impact H_2O_2 synthesis performance by enhancing the oxidative decomposition of H_2O_2 (Fig. 4*F*). This catalyzed H_2O_2 decomposition was minimized by separating H_2O_2 production centers (i.e., AQ) from Co decomposition sites, as indicated by much lower k_d in $Co_1/AQ/C_3N_4$ system as compared to Co_1/C_3N_4 system (Fig. 4*F*).

Results of our study suggest a facile strategy to anchor two spatially separated cocatalysts on a 2D photocatalyst. Such spatial separation ensures that the functions of both cocatalysts (i.e., Co_1 for enhanced water oxidation activity and AQ for improved H_2O_2 production selectivity) are fully utilized, resulting in additive enhancement in H_2O_2 photosynthesis. Here, atomic dispersion of metal cocatalyst presents advantage over conventional nanoparticles because the small size and strong ligand–metal coordination of single atom allow for facile manipulation of loading sites. The stark contrast on the performance of Co single atoms versus nanoparticles emphasizes the exclusive benefits of single atom catalysts in this material design. This center/edge strategy for loading two spatially separated cocatalysts may be also applicable on other 2D photocatalysts for achieving efficient charge separation while maintaining the effectiveness of both cocatalysts.

Methods

Preparation of Photocatalysts. Bulk C_3N_4 was prepared following a thermal polymerization procedure by heating melamine powder in a ceramic crucible at a heating rate of 1 °C/min to 550 °C and annealing for 5 h in a muffle furnace. As-prepared bulk C_3N_4 was grounded, exfoliated under probe sonication for 8 h, separated by centrifugation, washed with deionized water, and dried at 80 °C overnight. As-prepared ultrathin C_3N_4 (160 mg) was dispersed in 50 mL water under ultrasonication for 30 min, followed by addition of 1.5 mL $Co(NO_3)_2$ solution (2 g/L). The mixture was stirred and heated at 70 °C for 18 h, separated by centrifugation, dried at 80 °C overnight, and annealed at 400 °C for 2 h in a tube furnace under N_2 gas. The obtained powder was grounded, mixed with $NaPO_2{\bullet}H_2O$ (twice the weight of obtained powder), and heated at 300 °C for 2 h in a tube furnace under N_2 gas. As-prepared Co_1/C_3N_4 was washed with water and ethanol, and dried at 80 °C overnight. The Co loading amount was determined to be 0.13% (wt/wt; 0.34% of voids occupied) by inductively coupled plasma mass spectrometry (ICP-MS, PerkinElmer SCIEX Elan DRC-e) analysis after acid digestion. As-prepared Co_1/C_3N_4 (100 mg) was mixed with 10 mg anthraquinone-2-carboxylic acid, 7.7 mg diisopropylethylamine, 8.1 mg 1-hydroxybenzotriazole hydrate, and 11.5 mg *N*-(3-dimethylaminopropyl)-*N*′-ethylcarbodiimide hydrochloride. The mixture was dispersed in 50 mL dichloromethane under ultrasonication for 5 min and stirred for 48 h. The $Co_1/AQ/C_3N_4$ product was separated by centrifugation, washed with dichloromethane and water, and dried at 80 °C overnight. Co and AQ were loaded at a molar ratio of 1:37.

Catalyst Characterizations. HAADF-STEM images were taken using a Titan Themis Z STEM (ThermoFisher Scientific) operated at 200 kV, coupled with a probe aberration corrector to improve imaging spatial resolution to less than 1 Å. XPS measurements were performed with a Versa Probe II Scanning XPS Microprobe [Physical Electronics (PHI)]. We performed a survey analysis across the entire energy range and higher-resolution analyses in the N 1s, C 1s, P 2p, and O 1s regions. The XAS spectra at Co K edge were measured at Beamline 8-ID (ISS) of the National Synchrotron Light Source II (NSLS-II) at Brookhaven National Laboratory, using a Si (111) double-crystal monochromator and a passivated implanted planar silicon fluorescence detector. XANES data were collected at room temperature, with energy calibrated using Co foil. The P K-edge XAS data were collected at 8-BM of NSLS-II under fluorescence mode, employing a Si (111) crystals monochromator (45). Each sample was scanned for seven times to get better signal to noise ratio. Photoluminescence (PL) emission spectra were obtained using a fluorescence spectrophotometer (Shimadzu RF-5301). PL lifetime decays were measured by an inverted-type scanning confocal microscope (MicroTime-200, Picoquant) with a 20× objective. A single-mode pulsed diode laser (excitation wavelength at 375 nm with an instrumental response function of ~240 ps in pulse width) was used to as an excitation source to excite the samples coated on glass substrate. A dichroic mirror (490 DCXR, AHF), a long-pass filter (HQ500lp, AHF), and an avalanche photodiode detector (PDM series, MPD) were used to collect the entire emission (400–800 nm) from the samples. Photon counting and exponential fitting of the obtained PL decays were performed using the SymPhoTime software (version 5.3).

Photocatalytic Activity Tests. Photocatalytic production of H_2O_2 was assessed by irradiation of photocatalyst suspension (12 mL, 0.5 g/L) using a xenon lamp solar simulator (model 10500; Abet Technologies, Inc.). The light intensity was adjusted to 100 mW/cm^2 (AM 1.5G; irradiation area = 1.77 cm^2). The suspension was purged with O_2 before (for 5 min) and during irradiation. At designated time points, small aliquots from suspensions were taken for analysis of H_2O_2 productions.

Data Availability. All data of this study are included in the text and *SI Appendix*.

ACKNOWLEDGMENTS. This work was partially supported by National Science Foundation (NSF) Nanosystems Engineering Research Center for Nanotechnology-Enabled Water Treatment (Grant EEC-1449500). C.C. was financially supported by an Early Postdoctoral Mobility Fellowship, Swiss National Science Foundation (Award P2EZP2_168796) and D.H. was supported by the China Scholarship Council. We thank S. Zhuo and P. Wang at King Abdullah University of Science and Technology for STEM image analysis, J. Karosas at Yale University for ICP-MS analysis, and P. Kelleher at Yale University for help with XAFS sample preparation. We also thank D. Lu at Brookhaven National Laboratory (BNL) Center of Functional Materials for helpful discussions. This research used beamlines 8-BM and 8-ID (ISS) of the NSLS-II, US Department of Energy (DOE) Office of Science User Facilities operated for the DOE Office of Science by BNL under Contract DE-SC0012704. Computational work used the Extreme Science and Engineering Discovery Environment, supported by NSF (Grant ACI-1548562), through the Bridges high-performance computer at the Pittsburgh Supercomputing Center (Allocation ECD190001).

1. T. Hisatomi, J. Kubota, K. Domen, Recent advances in semiconductors for photocatalytic and photoelectrochemical water splitting. *Chem. Soc. Rev.* **43**, 7520–7535 (2014).
2. C. Chu *et al*., Electronic tuning of metal nanoparticles for highly efficient photocatalytic hydrogen peroxide production. *ACS Catal.* **9**, 626–631 (2019).
3. Y. Kofuji *et al*., Carbon nitride-aromatic diimide-graphene nanohybrids: Metal-free photocatalysts for solar-to-hydrogen peroxide energy conversion with 0.2% efficiency. *J. Am. Chem. Soc.* **138**, 10019–10025 (2016).
4. Y. Shiraishi *et al*., Resorcinol-formaldehyde resins as metal-free semiconductor photocatalysts for solar-to-hydrogen peroxide energy conversion. *Nat. Mater.* **18**, 985–993 (2019).
5. J. Liu *et al*., Water splitting. Metal-free efficient photocatalyst for stable visible water splitting via a two-electron pathway. *Science* **347**, 970–974 (2015).
6. Y. Goto *et al*., A particulate photocatalyst water-splitting panel for large-scale solar hydrogen generation. *Joule* **2**, 509–520 (2018).
7. X. Chen, S. Shen, L. Guo, S. S. Mao, Semiconductor-based photocatalytic hydrogen generation. *Chem. Rev.* **110**, 6503–6570 (2010).
8. W. J. Ong, L. L. Tan, Y. H. Ng, S. T. Yong, S. P. Chai, Graphitic carbon nitride ($g\text{-}C_3N_4$)-based photocatalysts for artificial photosynthesis and environmental remediation: Are we a step closer to achieving sustainability? *Chem. Rev.* **116**, 7159–7329 (2016).
9. D. Wang *et al*., Core/Shell photocatalyst with spatially separated co-catalysts for efficient reduction and oxidation of water. *Angew. Chem. Int. Ed. Engl.* **52**, 11252–11256 (2013).
10. K. Maeda *et al*., Photocatalytic overall water splitting promoted by two different cocatalysts for hydrogen and oxygen evolution under visible light. *Angew. Chem. Int. Ed. Engl.* **49**, 4096–4099 (2010).
11. S. S. K. Ma, K. Maeda, R. Abe, K. Domen, Visible-light-driven nonsacrificial water oxidation over tungsten trioxide powder modified with two different cocatalysts. *Energy Environ. Sci.* **5**, 8390–8397 (2012).
12. A. Li *et al*., Thin heterojunctions and spatially separated cocatalysts to simultaneously reduce bulk and surface recombination in photocatalysts. *Angew. Chem. Int. Ed. Engl.* **55**, 13734–13738 (2016).
13. D. Zheng, X. N. Cao, X. Wang, Precise formation of a hollow carbon nitride structure with a Janus surface to promote water splitting by photoredox catalysis. *Angew. Chem. Int. Ed. Engl.* **55**, 11512–11516 (2016).
14. M. Xing *et al*., Spatially separated CdS shells exposed with reduction surfaces for enhancing photocatalytic hydrogen evolution. *Adv. Funct. Mater.* **27**, 1702624–1702634 (2017).
15. J. Zhang *et al*., Porous TiO_2 nanotubes with spatially separated platinum and CoO_x cocatalysts produced by atomic layer deposition for photocatalytic hydrogen production. *Angew. Chem. Int. Ed. Engl.* **56**, 816–820 (2017).
16. R. Li *et al*., Spatial separation of photogenerated electrons and holes among 010 and 110 crystal facets of BiVO4. *Nat. Commun.* **4**, 1432–1439 (2013).
17. R. G. Li, H. X. Han, F. X. Zhang, D. G. Wang, C. Li, Highly efficient photocatalysts constructed by rational assembly of dual-cocatalysts separately on different facets of $BiVO_4$. *Energy Environ. Sci.* **7**, 1369–1376 (2014).
18. A. Meng, J. Zhang, D. Xu, B. Cheng, J. Yu, Enhanced photocatalytic H_2-production activity of anatase TiO_2 nanosheet by selectively depositing dual-cocatalysts on {101} and {001} facets. *Appl. Catal. B* **198**, 286–294 (2016).
19. Y. Shiraishi *et al*., Sunlight-driven hydrogen peroxide production from water and molecular oxygen by metal-free photocatalysts. *Angew. Chem. Int. Ed. Engl.* **53**, 13454–13459 (2014).
20. Y. Kofuji *et al*., Graphitic carbon nitride doped with biphenyl diimide: Efficient photocatalyst for hydrogen peroxide production from water and molecular oxygen by sunlight. *ACS Catal.* **6**, 7021–7029 (2016).
21. K. Mase, M. Yoneda, Y. Yamada, S. Fukuzumi, Seawater usable for production and consumption of hydrogen peroxide as a solar fuel. *Nat. Commun.* **7**, 11470–11476 (2016).
22. Y. Shiraishi *et al*., Highly selective production of hydrogen peroxide on graphitic carbon nitride (gC_3N_4) photocatalyst activated by visible light. *ACS Catal.* **4**, 774–780 (2014).
23. H.-i. Kim, Y. Choi, S. Hu, W. Choi, J.-H. Kim, Photocatalytic hydrogen peroxide production by anthraquinone-augmented polymeric carbon nitride. *Appl. Catal. B* **229**, 121–129 (2018).
24. Y. Shiraishi *et al*., Effects of surface defects on photocatalytic H_2O_2 production by mesoporous graphitic carbon nitride under visible light irradiation. *ACS Catal.* **5**, 3058–3066 (2015).
25. G.-h. Moon *et al*., Eco-friendly photochemical production of H_2O_2 through O_2 reduction over carbon nitride frameworks incorporated with multiple heteroelements. *ACS Catal.* **7**, 2886–2895 (2017).
26. D. K. Zhong, D. R. Gamelin, Photoelectrochemical water oxidation by cobalt catalyst ("Co-Pi")/α-$Fe(_2)O(_3)$ composite photoanodes: Oxygen evolution and resolution of a kinetic bottleneck. *J. Am. Chem. Soc.* **132**, 4202–4207 (2010).
27. M. Barroso *et al*., The role of cobalt phosphate in enhancing the photocatalytic activity of α-Fe_2O_3 toward water oxidation. *J. Am. Chem. Soc.* **133**, 14868–14871 (2011).
28. R. S. Khnayzer *et al*., Structure and activity of photochemically deposited "CoPi" oxygen evolving catalyst on titania. *ACS Catal.* **2**, 2150–2160 (2012).
29. G. H. Moon, W. Kim, A. D. Bokare, N. E. Sung, W. Choi, Solar production of H_2O_2 on reduced graphene oxide-TiO_2 hybrid photocatalysts consisting of earth-abundant elements only. *Energy Environ. Sci.* **7**, 4023–4028 (2014).
30. M. W. Kanan, Y. Surendranath, D. G. Nocera, Cobalt-phosphate oxygen-evolving compound. *Chem. Soc. Rev.* **38**, 109–114 (2009).
31. J. M. Campos-Martin, G. Blanco-Brieva, J. L. G. Fierro, Hydrogen peroxide synthesis: An outlook beyond the anthraquinone process. *Angew. Chem. Int. Ed. Engl.* **45**, 6962–6984 (2006).
32. X. Zhang *et al*., Enhanced photoresponsive ultrathin graphitic-phase C3N4 nanosheets for bioimaging. *J. Am. Chem. Soc.* **135**, 18–21 (2013).
33. W. Liu *et al*., Single-site active cobalt-based photocatalyst with a long carrier lifetime for spontaneous overall water splitting. *Angew. Chem. Int. Ed. Engl.* **56**, 9312–9317 (2017).
34. Y. Zheng *et al*., Molecule-level $g\text{-}C_3N_4$ coordinated transition metals as a new class of electrocatalysts for oxygen electrode reactions. *J. Am. Chem. Soc.* **139**, 3336–3339 (2017).
35. F. K. Kessler *et al*., Functional carbon nitride materials-design strategies for electrochemical devices. *Nat. Rev. Mater.* **2**, 17030–17047 (2017).
36. M. W. Kanan, D. G. Nocera, In situ formation of an oxygen-evolving catalyst in neutral water containing phosphate and Co^{2+}. *Science* **321**, 1072–1075 (2008).
37. R. Chen *et al*., Charge separation via asymmetric illumination in photocatalytic Cu_2O particles. *Nat. Energy* **3**, 655–663 (2018).
38. Q. Zhang *et al*., Effect of redox cocatalysts location on photocatalytic overall water splitting over cubic $NaTaO_3$ semiconductor crystals exposed with equivalent facets. *ACS Catal.* **6**, 2182–2191 (2016).
39. S. T. Oyama, P. Clark, V. L. S. Teixeira da Silva, E. J. Lede, F. G. Requejo, XAFS characterization of highly active alumina-supported molybdenum phosphide catalysts (MoP/Al_2O_3) for hydrotreating. *J. Phys. Chem. B* **105**, 4961–4966 (2001).
40. Z. Shi *et al*., Phosphorus-Mo_2C@Carbon nanowires toward efficient electrochemical hydrogen evolution: Composition, structural and electronic regulation. *Energy Environ. Sci.* **10**, 1262–1271 (2017).
41. J. Xue, S. Ma, Y. Zhou, Z. Zhang, M. He, Facile photochemical synthesis of Au/Pt/$g\text{-}C_3N_4$ with plasmon-enhanced photocatalytic activity for antibiotic degradation. *ACS Appl. Mater. Interfaces* **7**, 9630–9637 (2015).
42. J. Mao *et al*., Accelerating water dissociation kinetics by isolating cobalt atoms into ruthenium lattice. *Nat. Commun.* **9**, 4958–4966 (2018).
43. H. Hirakawa *et al*., Au nanoparticles supported on $BiVO_4$: Effective inorganic photocatalysts for H_2O_2 production from water and O_2 under visible light. *ACS Catal.* **6**, 4976–4982 (2016).
44. F. Shiraishi, T. Nakasako, Z. Z. Hua, Formation of hydrogen peroxide in photocatalytic reactions. *J. Phys. Chem. A* **107**, 11072–11081 (2003).
45. P. Northrup, The TES beamline (8-BM) at NSLS-II: Tender-energy spatially resolved X-ray absorption spectroscopy and X-ray fluorescence imaging. *J. Synchrotron Radiat.* **26**, 2064–2074 (2019).